The Effect of Acoustic Disturbances on the Operation of the Space Shuttle Main Engine Fuel Flowmeter.

Authors:

Bogdan Marcu
Roland Szabo
Pratt and Whitney Rocketdyne
Canoga Park, CA

Dan Dorney
Tom Zoladz
NASA
George C. Marshall Space Flight Center
MSFC, AL

Abstract

The Space Shuttle Main Engine (SSME) uses a turbine fuel flowmeter (FFM) in its Low Pressure Fuel Duct (LPFD) to measure liquid hydrogen flowrates during engine operation. The flowmeter is required to provide accurate and robust measurements of flow rates ranging from 10000 to 18000 GPM in an environment contaminated by duct vibration and duct internal acoustic disturbances. Errors exceeding 0.5% can have a significant impact on engine operation and mission completion. The accuracy of each sensor is monitored during hot-fire engine tests on the ground. Flow meters which do not meet requirements are not flown. Among other parameters, the device is screened for a specific behavior in which a small shift in the flow rate reading is registered during a period in which the actual fuel flow as measured by a facility meter does not change. Such behavior has been observed over the years for specific builds of the FFM and must be avoided or limited in magnitude in flight. Various analyses of the recorded data have been made prior to this report in an effort to understand the cause of the phenomenon; however, no conclusive cause for the shift in the instrument behavior has been found.

The present report proposes an explanation of the phenomenon based on interactions between acoustic pressure disturbances in the duct and the wakes produced by the FFM flow straightener. Physical insight into the effects of acoustic plane wave disturbances was obtained using a simple analytical model. Based on that model, a series of three-dimensional unsteady viscous flow computational fluid dynamics (CFD) simulations were performed using the MSFC PHANTOM turbomachinery code. The code was customized to allow the FFM rotor speed to change at every time step according to the instantaneous fluid forces on the rotor, that, in turn, are affected by acoustic plane pressure waves propagating through the device.

The results of the simulations show the variation in the rotation rate of the flowmeter due to the interaction of the flow straightener wakes and the upstream propagating acoustic waves. A detailed analysis of the acoustic disturbance effects is presented along with an assessment of the impact on measurement accuracy.

1. Introduction

The Space Shuttle Main Engine uses a turbine type Fuel Flow Meter [1] to measure the amount of fuel delivered to the engine and to thereby control the engine oxidizer/fuel mixture ratio. The flow meter is located in the Low Pressure Fuel Duct that connects the Low Pressure Fuel Pump discharge to the High Pressure Fuel Pump inlet. The meter converts rotor speed to volumetric flow rate through the proportionality relationship $K_f = 4RPM / GPM$, where RPM is the rotor speed in rotations per minute; GPM the fuel volumetric flow rate in gallons per minute; and K_f is a proportionality constant.

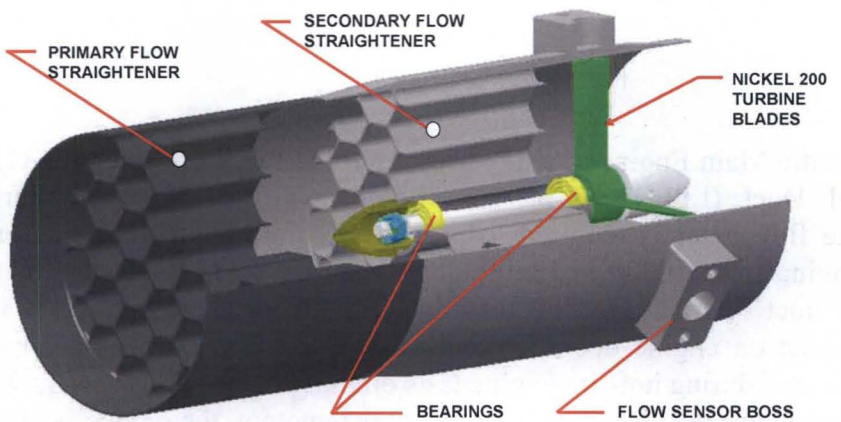

Figure 1. SSME Fuel Flow Meter Configuration

The flow meter, shown in Fig. 1, consists of a set of honeycomb flow straighteners, followed by a 4-blade turbine rotor. The rotor's speed of rotation is picked up by a magnetic sensor.

The flowmeter is preliminarily calibrated in a water flow test, and subsequently re-calibrated on engine during a ground green-run test. During ground tests, is has been observed that particular builds of the flowmeter exhibit a small shift in the calibration constant during engine operation [2, 3]. This is evidenced by an apparent change in the reported flow rate, without a real change in the actual flow rate as measured by a facility flow meter and as corroborated by observation of other engine parameters. The detailed plot of the onset of the anomalous behavior shows that while the real volume flow (denoted as facility flow) decreases slightly, the flowmeter indicates a slight increase. In many but not all of these occurrences, the onset of the shifted calibration value is associated with significant fluctuations in the flowmeter speed, as shown in Fig. 3. The true frequency of the rotor speed fluctuation cannot be determined since the rotation speed sampled at only 4 times per revolution and the measurement would thus be affected by aliasing.

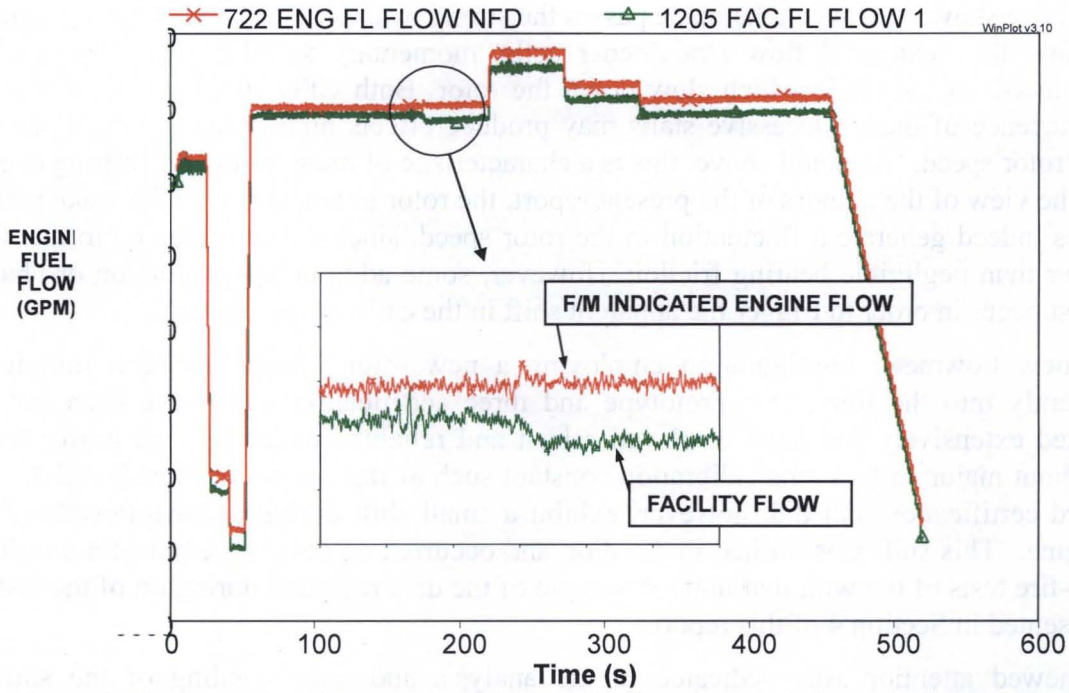

Figure 2. An example of an apparent shift of the flowmeter's indication during ground testing.

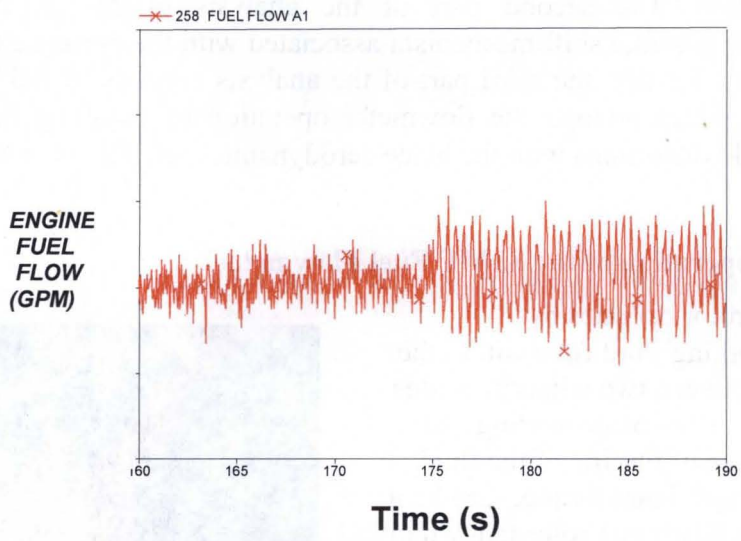

Figure 3. In most but not all of the cases of K_f shifting, the onset of the K_f apparent value shift is associated with oscillations in the flowmeter's reading.

Several authors have investigated this phenomenon. The effects of engine vibrations on the duct flow have been assessed without finding conclusive evidence of a possible significant effect [2]. Another analysis [4] has demonstrated that the rotor's sensitivity to turbulence intensity is uncorrelated to the shift in the calibration constant. Unsteady 2-D CFD analysis by A. Hadid [6], and pseudo-unsteady 3-D CFD analysis by E. Ascoli et.al.

[5] have shown that when the blade passes the strong wakes in the flow pattern generated behind the hexagonal flow straightener cells, momentary stall-like flow features are produced on the blade which slow down the rotor. Both CFD studies suggest that the occurrence of these successive stalls may produce effects high frequency oscillation of the rotor speed. As noted above, this is a characteristic of many of the Kf shifting events. In the view of the authors of the present report, the rotor interaction with the wake pattern does indeed generate a fluctuation in the rotor speed, since the rotor has no torque load other than negligible bearing friction. However, some additional perturbation or change must occur in order to trigger the apparent shift in the calibration constant.

A new flowmeter configuration employing a new rotor design has been introduced recently into the fleet. One prototype and three certification units have been hot-fire tested extensively and have displayed robust and reliable operation at all power levels without major shifts in the calibration constant such as that shown in Figs. 2 and 3. The third certification unit did, however, exhibit a small shift during a down-throttle of the engine. This shift was limited in duration and occurred on only three out of a multitude hot-fire tests of the with that unit. A sample of the data recorded during on of the tests is presented in Section 4 of this report.

Renewed attention was dedicated to the analysis and understanding of the shifting phenomenon. The present report focuses on the effects of acoustic wave perturbations generated by the High Pressure Fuel Pump that propagate upstream in the Low Pressure Fuel Duct towards the Fuel Flowmeter. The first part of the analysis presented establishes the parameters and characteristics of the flow meter operation in the absence of any perturbation. The second part of the analysis establishes the theoretical background for the possible shift mechanism associated with the presence of the acoustic wave perturbations. Finally, the third part of the analysis consists of full 3-D, unsteady CFD simulations which address the flowmeter operation by coupling the acoustically disturbed flow field distortions with the blade aerodynamics and the rotor inertia

2. Quasi-steady operation of the SSME Fuel Flowmeter

A typical turbine rotor operates by organizing the working fluid flow within the channel formed between two adjacent blades in a way that maximizes blade loading and allows a high degree of turning of the fluid, thus producing a significant torque. Unlike a power turbine, the flowmeter rotor (shown in Fig. 4) uses only 4 blades that operate practically independent of each other as isolated rotating airfoils. If the rotor were to operate in a smooth, uniform incoming flow, each of its blades should operate at very small incidence angles at every radius. The situation is depicted in Fig. 5. The incoming flow has a uniform axial velocity C_a while

Figure 4. The flow meter rotor.

the rotor blade has the tangential velocity U as shown. Adding the two vector velocities results in the relative velocity with respect to the blade, W. The blade stagger angle α is not quite aligned with the relative velocity angle β as the relative velocity impinges on the blade's leading edge at a small incidence angle *i*. Since the blade profile is symmetric, a small incidence angle is necessary to produce some lift besides drag. For our analysis, only the tangential components of the forces acting on the rotor blade are of interest. The blade will adjust its tangential velocity in a way that will produce a very small incidence angle *i* for which the tangential component of the drag force and rotor miscellaneous friction resistances R_f will be compensated by the tangential component of lift. Due to the free-vortex blade twist $\alpha = \alpha(R)$ (Figs. 5b and 5c), this situation occurs at every radius R of the blade.

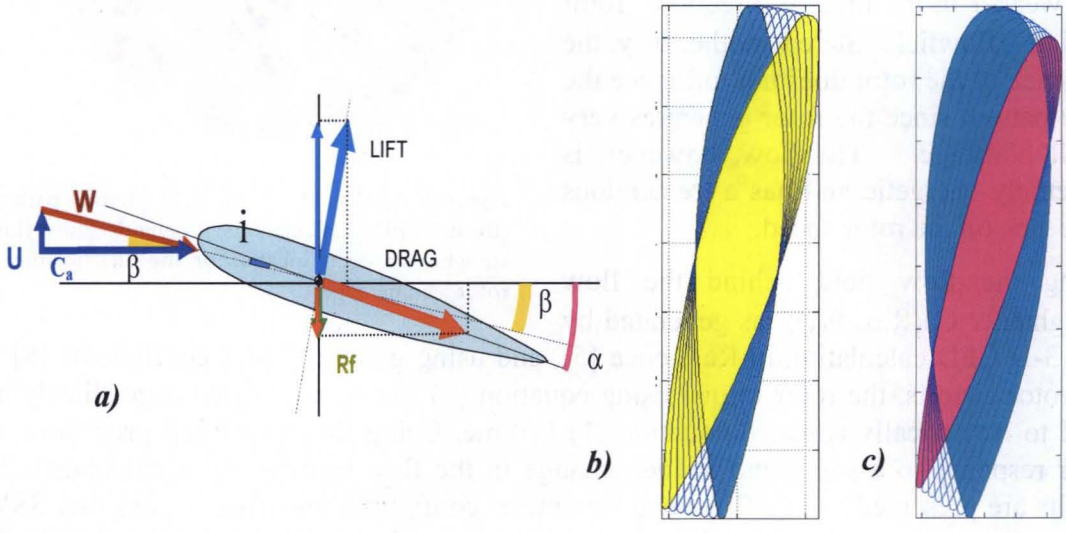

Figure 5. a) The blade load and force decomposition on the rotor, b) blade airfoil and twist for the original rotor design and c) new rotor design

The incoming flow, however, is not uniform. The hexagonal channels of the straightener generate a flow pattern as shown in Fig. 6. The pattern is periodic in the tangential direction, characterized by 6N, 12N and 18 N periodicity in circumferential direction. In the model shown in Fig. 5 the axial fluid velocity becomes a forcing function $C_a=C_a(t)$, since the rotor will "feel" an unsteady axial velocity as it passes through the wakes in the flow pattern behind the flow straightener. For a rotor with a mass moment of inertia *I*, at every moment in time its motion is governed by the dynamic equation of motion:

$$I\frac{d^2\theta(t)}{dt^2} = T[\theta(t), \alpha(R), C(R, \alpha, \theta(t))] \qquad (1)$$

where $\theta = \theta(t)$ is the rotor's angular position, t is the time, and T is the torque produced by the resultant force on the blade according the model in Fig. 5, i.e.,

$$T = T[\theta(t), \alpha(R), Ca(R, \alpha, \theta(t))]. \qquad (2)$$

The torque equation (2) expresses simultaneous, nonlinear, two-way coupling between the rotor position and the aerodynamic forces on the blade. In order to solve the dynamic

equation of motion, one must rely on numerical simulations in which equation (1) is coupled to a 3-D viscous, unsteady flow solver. This formalism is the basis for the calculations presented in Section 5. Before launching into expensive and time consuming numerical simulations, however, insight was gained using a simplified algorithm employing the assumption that the coupling between the wake and the rotor is stronger in the forward direction: flowfield→rotor motion and weaker in the reverse direction: rotor motion→flowfield Stated another way, the presence of the rotor does not influence the flow pattern since the rotor generates very small blockage. The flow, however, is extremely energetic and has a tremendous influence on the rotor speed.

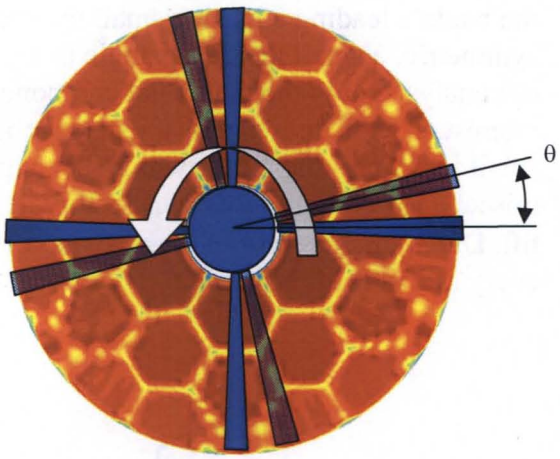

Figure 6. Axial fluid velocity field intensity pattern (from CFD calculations) behind the flow straightener at the location of the fuel flowmeter rotor leading edge.

Using the flow field behind the flow straightener $Ca(R,\alpha, \theta(t))$ as generated by the 3-D CFD calculation in Reference [5], and using generic C_D/C_L coefficients [8] for the rotor airfoils, the rotor torque using equation (2) can be calculated immediately and used to numerically advance equation (1) in time. Using this simplified procedure, the rotor response to a small and sudden change in the flow rate has been calculated. The results are presented in Fig. 7 for two flowmeter configurations using the orginial SSME flowmeter rotor with I=0.0035 lbm ft^2, and the new redesigned rotor with I=0.0039 lbm ft^2.

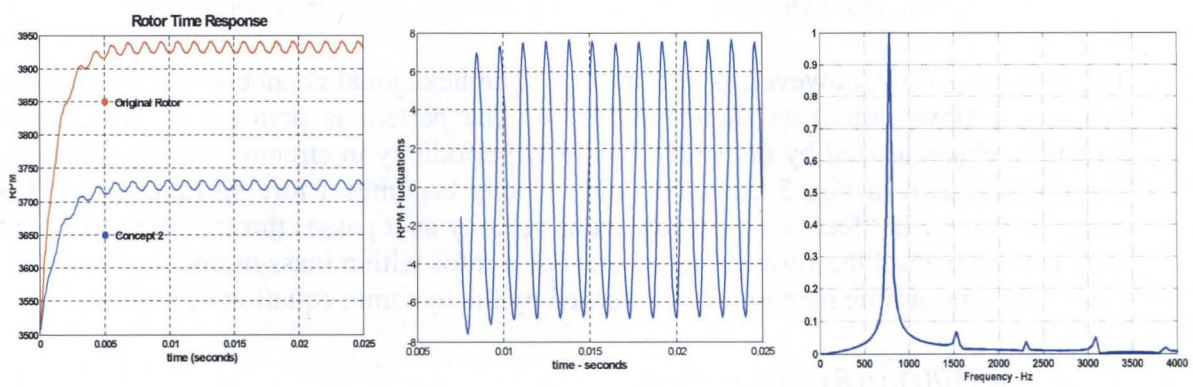

(a) *(b)* *(c)*

Figure 7. a) Rotor time response to a change in flow volumetric rate. b) Rotor speed fluctuation component during quasi-steady operation. c) spectral analysis of the fluctuating component: the peak corresponds to 12N frequency.

The simulation results confirm the measured response time, which is of the order of 6 milliseconds for both rotors. One important detail can be observed: after the rotor

responds to a change in the volumetric flow rate, it operates in a quasi-steady regime characterized by stable and periodic speed fluctuations of very small amplitude. The amplitude of the fluctuations shown is 0.28% and 0.21% of the mean speed value for the original and the new design, respectively. Figure 7b shows the fluctuating component of the rotor speed for the original rotor, calculated for fuel volumetric flow at 115% engine RPL. The spectral analysis of the fluctuation is shown in Fig. 7c. The dominant frequency (791 Hz) corresponds to the 12N symmetry of the hexagonal flow straightener pattern.

The result of this calculation has led to the hypothesis that the random and sudden shifts in the value of the calibration constant for the flowmeter are somehow related to the small fluctuation in the rotor's speed. If the duct flow was free of wakes, especially of wakes in periodic patterns, shifts in the calibration constant value would not occur.

Nevertheless, some additional factor must be present in order to trigger the shift in the average rotor speed. The additional factor, whatever it may be, must be able to interact with the wakes in a manner correlated well enough to trigger a significant change in rotor airfoil performance, or some other effect with the same equivalent result: a sudden change in the rotor average speed.

3. Simple Analytical Model of Effect of Acoustic Plane Wave on Flowmeter

The additional disturbance factor in the above hypothesis might be provided by an acoustic pressure wave propagating upstream through the fuel duct as a result of cavitation phenomena occurring at the inlet of the High Pressure Fuel Turbo Pump (HPFTP). Such acoustic disturbances are generated at various frequencies by the pump. A theoretical model of the effect of an acoustic plane wave on the flowmeter has been constructed and is described as follows:

Two reference frames are considered in this model. The first is referred to as the absolute reference frame. This is the reference frame in which the duct that contains the flowmeter and the straightener vanes that are upstream of the rotor are stationary. The second is the relative reference frame. This is the reference frame in which the rotor appears stationary.

In the absolute reference frame, the axial velocity just downstream of the straightener vanes can be expressed as a spatial Fourier series:

$$u(r,\theta_s) = u_0 + u_1(r)\cos 6\theta_s + u_2(r)\cos 12\theta_s + \ldots$$

where θ_s is measured in the absolute frame with respect to a fixed point on the flow straightener (say, top dead center of the duct). Positive θ_s is taken to be in the direction of rotation of the rotor. Only the 6, 12, … terms appear in the Fourier series because of the 6, 12, … sequences in the straightener vane pattern. The Fourier coefficients are each a function of radius, r. In reality, there would most likely be *sine* terms as well as *cosine* terms in the Fourier series of the straightener discharge velocity. Since the model being described here is used only for pedagogical rather than quantitative purposes, the *sine* terms have been omitted. At any point in space, the straightener discharge velocity is

steady in the absolute reference frame. For now, steady flow in the duct with no acoustic disturbances is assumed.

In order to go from the absolute to the relative frame of reference, the following substitution is made:

$$\theta_s = \theta_r + \Omega t \quad .$$

where θ_r is measured in the relative frame with respect to a fixed point on the rotor (say, Blade A). The rotor shaft speed in radians per second is Ω. Using this convention, θ_r = 0 deg on Blade A, θ_r = 90 deg on Blade B, θ_r = 180 deg on Blade C, θ_r = 270 deg on Blade D. We assume θ_r also increases in the direction of rotation. The order in which blades pass a fixed point on the duct is D, C, B, A, D, …

In the relative frame of reference, the axial velocity just downstream of the straightener vanes is

$$u(r,\theta_s) = u_0 + u_1(r)\cos 6(\theta_r + \Omega t) + u_2(r)\cos 12(\theta_r + \Omega t_s) + ...$$

Notice that since $\theta_r = \theta_s - \Omega t$, we would need to travel backwards with respect to the rotor in order to be stationary with respect to the straightener vanes.

Other than a small amount of bearing friction, there is nothing to resist the torque imparted by the flow over the rotor. As a result, for a given steady flowrate, the rotor spins at a speed that results in a near zero incidence angle on the blades as explained in Section 2. The blades, of course, are twisted so that the incidence angle is nearly zero over their full span as shown in Figs. 5b and 5c. Ideally, the rotor speed is proportional to the axial velocity incident to the rotor.

If the flow is unsteady with respect to the blades, then the rotor will speed up or slow down according to the instantaneous torque on the rotor and the inertia of the rotor as shown in Fig. 7. The rotor does in fact see oscillations in incoming axial velocity as it passes through the straightener wakes. In the simple development put forth in this section, the rotor inertia is assumed to be negligible so that the rotor speed follows changes in flow torque instantaneously. With this assumption, the following linearization of the fluctuating component of rotor speed due to its passage through the straightener wakes can be obtained:

$$\begin{aligned}
\tilde{\Omega}(t) = A\int_{Rhub}^{Rtip}\left(ru_1(r)\cos 6(0+\Omega t) + ru_2(r)\cos 12(0+\Omega t_s) + ...\right)dr \\
+ A\int_{Rhub}^{Rtip}\left(ru_1(r)\cos 6(\pi/2+\Omega t) + ru_2(r)\cos 12(\pi/2+\Omega t_s) + ...\right)dr \\
+ A\int_{Rhub}^{Rtip}\left(ru_1(r)\cos 6(\pi+\Omega t) + ru_2(r)\cos 12(\pi+\Omega t_s) + ...\right)dr \\
+ A\int_{Rhub}^{Rtip}\left(ru_1(r)\cos 6(3\pi/2+\Omega t) + ru_2(r)\cos 12(3\pi/2+\Omega t_s) + ...\right)dr
\end{aligned}$$

Here, the four integrals represent the sum of the moments about the shaft centerline exerted by the flow over the four blades. The constant 'A' that includes density, blade geometry, and other factors.

In the following rearranged expression, it is easy to see that the net rotor torques produced by the $6\theta_s$, $18\theta_s$, $30\theta_s$, ... components of the straightener wakes cancel one another while the net rotor torques produced by the $12\theta_s$, $24\theta_s$, $36\theta_s$, ... remain:

$$\begin{aligned}\tilde{\Omega}(t) = {} & A\left(\cos 6(0+\Omega t)+\cos 6(\pi/2+\Omega t)+\cos 6(\pi+\Omega t)+\cos 6(3\pi/2+\Omega t)\right)\int_{Rhub}^{Rtip} ru_1(r)dr \\ & + A\left(\cos 12(0+\Omega t)+\cos 12(\pi/2+\Omega t)+\cos 12(\pi+\Omega t)+\cos 12(3\pi/2+\Omega t)\right)\int_{Rhub}^{Rtip} ru_1(r)dr \\ & + A\left(\cos 18(0+\Omega t)+\cos 18(\pi/2+\Omega t)+\cos 18(\pi+\Omega t)+\cos 18(3\pi/2+\Omega t)\right)\int_{Rhub}^{Rtip} ru_1(r)dr \\ & + A\left(\cos 24(0+\Omega t)+\cos 24(\pi/2+\Omega t)+\cos 24(\pi+\Omega t)+\cos 24(3\pi/2+\Omega t)\right)\int_{Rhub}^{Rtip} ru_1(r)dr \\ & + \ldots\end{aligned}$$

Note that each rotor blade is still subject to pressure pulses at 6, 12, 18, 24, ... times shaft speed. However, the contributions of adjacent blades to the net rotor torque cancel at these harmonics. As a result, the rotor speed harmonics produced by this straightener appear only at 12, 24, 36, ... time shaft speed:

$$\tilde{\Omega}(t) = 4A\cos 12\Omega t\int_{Rhub}^{Rtip} ru_2(r)dr + 4A\cos 24\Omega t\int_{Rhub}^{Rtip} ru_4(r)dr + 4A\cos 36\Omega t\int_{Rhub}^{Rtip} ru_6(r)dr + \ldots$$

In the discussion thus far, the flow leaving the straightener vanes has been assumed to be steady in the absolute frame of reference. Now, however, the effect of an extraneous traveling acoustic plane wave superimposed on the steady flow will be considered.

Far upstream of the straightener vanes, the flow velocity in the absolute reference frame is:

$$u(r,\theta_s,t) = u_0(1+\varepsilon\cos\omega_{ac}t)$$

The frequency of the acoustic wave is ω_{ac} radians per second. The product $u_0\varepsilon$ is the amplitude of the acoustic particle velocity:

$$u' = u_0\varepsilon = \frac{p'}{\rho c}$$

In the present problem, the product $u_0\varepsilon$ may also represent the fluctuation in straightener wake thickness due to the fluctuating pressure drop across the straightener. Over the course of an acoustic cycle, the instantaneous pressure drop across the straightener ranges from more favorable than average to more adverse than average. It is suggested here that this may affect the boundary layers growing on the straightener vanes

and thus the characteristics of the wakes downstream of the straightener vanes. This second interpretation is suggested because, for acoustic fluctuating pressure amplitudes at the frequencies of interest to the present problem, the corresponding particle velocity given by equation u'=p'/□c would be quite small.

Downstream of the straightener vanes, the flow velocity in the absolute reference frame is:

$$u(r,\theta_s,t) = u_0(1+\varepsilon_0\cos\omega_{ac}t) + u_1(r)(1+\varepsilon_1\cos\omega_{ac}t)\cos 6\theta_s + u_2(r)(1+\varepsilon_2\cos\omega_{ac}t)\cos 12\theta_s + \ldots$$

The acoustic plane wave perturbs not only the spatial mean velocity (u_0) but all of the higher spatial orders of the straightener vanes, too. The products $u_1(r)\varepsilon_1$, $u_1(r)\varepsilon_1$, etc, include the effect of the fluctuation in boundary layer thickness over the straightener vanes (and thus, the straightener wake thickness) due to the fluctuating pressure drop across the straightener.

The transition from the absolute to the relative reference frame is made once again:

$$\begin{aligned} u(r,\theta_s,t) = {} & u_0(1+\varepsilon_0\cos\omega_{ac}t) \\ & + u_1(r)(1+\varepsilon_1\cos\omega_{ac}t)\cos 6(\theta_r+\Omega t) \\ & + u_2(r)(1+\varepsilon_2\cos\omega_{ac}t)\cos 12(\theta_r+\Omega t) + \ldots \end{aligned}$$

Neglecting rotor inertia, the fluctuating component of rotor speed is taken to be proportional, once again, to the fluctuating components of axial velocity at θ_r = 0, $\pi/2$, π, and 3 $\pi/2$ radians, added together:

$$\begin{aligned} \tilde{\Omega}(t) = {} & A(1+\varepsilon_0\cos\omega_{ac}t)\int_{Rhub}^{Rtip} r u_0(r)dr \\ & + A\sum_i \int_{Rhub}^{Rtip} r u_i(r)(1+\varepsilon_i\cos\omega_{ac}t)\cos 6i(0+\Omega t)dr \\ & + A\sum_i \int_{Rhub}^{Rtip} r u_i(r)(1+\varepsilon_i\cos\omega_{ac}t)\cos 6i(\pi/2+\Omega t)dr \\ & + A\sum_i \int_{Rhub}^{Rtip} r u_i(r)(1+\varepsilon_i\cos\omega_{ac}t)\cos 6i(\pi+\Omega t)dr \\ & + A\sum_i \int_{Rhub}^{Rtip} r u_i(r)(1+\varepsilon_i\cos\omega_{ac}t)\cos 6i(3\pi/2+\Omega t)dr \end{aligned}$$

As before, the net rotor torques produced by the $6\theta_s$, $18\theta_s$, $30\theta_s$, … components of the straightener wakes cancel out while the net rotor torques produced by the $12\theta_s$, $24\theta_s$, $36\theta_s$, … remain:

$$\tilde{\Omega}(t) = A(1+\varepsilon_0 \cos\omega_{ac} t)\int_{Rhub}^{Rtip} ru_0(r)dr$$
$$+4A(1+\varepsilon_2 \cos\omega_{ac} t)\cos 12\Omega t \int_{Rhub}^{Rtip} ru_2(r)dr$$
$$+4A(1+\varepsilon_4 \cos\omega_{ac} t)\cos 24\Omega t \int_{Rhub}^{Rtip} ru_4(r)dr$$
$$+4A(1+\varepsilon_6 \cos\omega_{ac} t)\cos 36\Omega t \int_{Rhub}^{Rtip} ru_6(r)dr + \ldots$$

The only addition is the spatial mean ($0\theta_s$) term.

Use of the product of cosines identity reveals the frequencies at which rotor speed is expected to oscillate under the combined influence of straightener wakes and an acoustic plane wave:

$$\tilde{\Omega}(t) = A(1+\varepsilon_0 \cos\omega_{ac} t)\int_{Rhub}^{Rtip} ru_0(r)dr$$
$$+4A\left(\cos 12\Omega t + \frac{\varepsilon_2}{2}\cos(\omega_{ac}-12\Omega)t + \frac{\varepsilon_2}{2}\cos(\omega_{ac}+12\Omega)t\right)\int_{Rhub}^{Rtip} ru_2(r)dr$$
$$+4A\left(\cos 24\Omega t + \frac{\varepsilon_4}{2}\cos(\omega_{ac}-24\Omega)t + \frac{\varepsilon_4}{2}\cos(\omega_{ac}+24\Omega)t\right)\int_{Rhub}^{Rtip} ru_4(r)dr$$
$$+4A\left(\cos 36\Omega t + \frac{\varepsilon_6}{2}\cos(\omega_{ac}-36\Omega)t + \frac{\varepsilon_6}{2}\cos(\omega_{ac}+36\Omega)t\right)\int_{Rhub}^{Rtip} ru_6(r)dr$$
$$+\ldots$$

The foregoing expression shows that rotor speed oscillations should be expected at the following frequencies (in radians per second):

	ω_{ac}	
12Ω	$\omega_{ac}-12\Omega$	$\omega_{ac}+12\Omega$
24Ω	$\omega_{ac}-24\Omega$	$\omega_{ac}+24\Omega$
36Ω	$\omega_{ac}-36\Omega$	$\omega_{ac}+36\Omega$
etc		

Particularly interesting are those cases when the frequency of the extraneous acoustic wave ω_{ac} gradually approaches and then crosses one of the straightener vane harmonic frequencies 12Ω, etc. Rotor speed dither would occur at a frequency equal to the progressively decreasing difference of the acoustic and vane harmonic frequencies. At the point when these two frequencies became equal, the pertinent term in the rotor speed oscillation expression would actually represent a shift in rotor speed. For example, if extraneous acoustic plane wave energy is present at 12 times flowmeter rotor speed, then

the expression for the perturbation in rotor speed would include the following shift in steady rotor speed:

$$\tilde{\Omega}_{shift} = 2A\varepsilon_2 \int_{Rhub}^{Rtip} ru_2(r)dr$$

4. Potential Evidence of Flowmeter Excursion Due to Acoustic Plane Wave Interaction During SSME Hotfire Test

Dynamic data from several SSME static firings were evaluated by the authors in light of the acoustic disturbance theory. Dynamic data were available from LPFD (low pressure fuel duct) fluctuating pressures, accelerometers and strain gages. Dynamic data were also available from housing accelerometers on both the low and high pressure fuel turbopumps, for which the duct serves as a propellant conduit. The dynamic data were used to identify frequencies of potential planar LPFP acoustics. Instances where these frequencies were aligned with upstream straightener vane wake harmonics, as observed by the flowmeter rotor, were sought out. Correlations between these instances of alignment and observed flowmeter shifts were then attempted.

Figure 8 is a spectrogram of LPFD radial acceleration at the fuel flow meter acquired during an SSME ground test. Circled are time-frequency regions of interest where acceleration blossoms might indicate the existence of planar acoustic waves propagating within the duct. The "three-pronged" spectral pattern has been attributed to the interaction of a sub-synchronous stall disturbance with the high pressure fuel turbopump 6-bladed impeller.

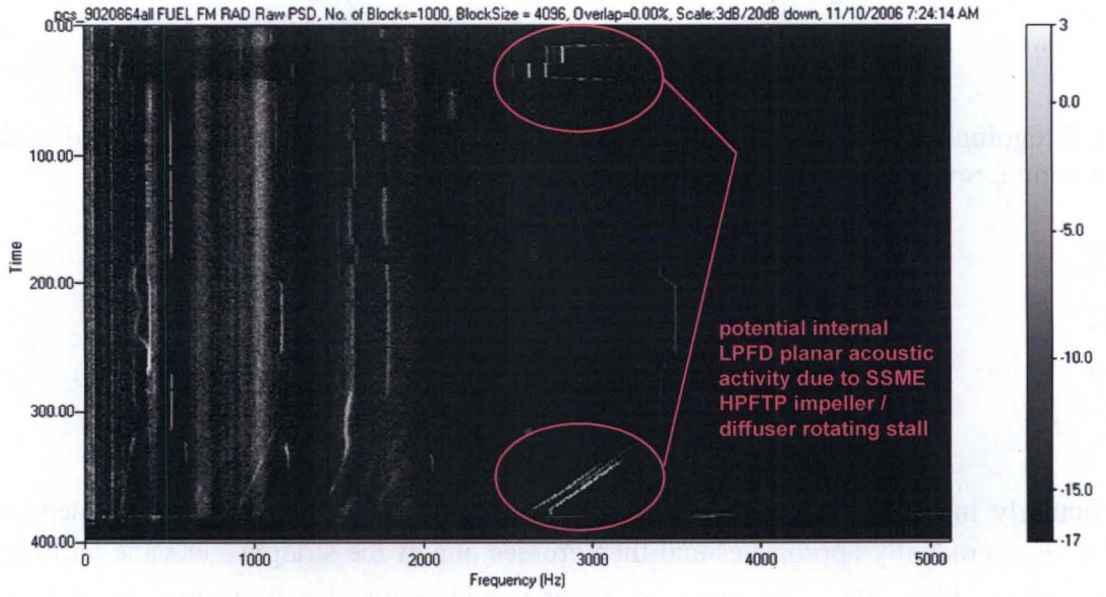

Figure 8. Spectrogram of Low Pressure Fuel Duct Fuel Flow Meter Acceleration.

Figure 9 displays temporal traces corresponding to engine-to-facility flow ratio, FFM radial acceleration, the frequency associated with the tracked FFM radial acceleration at

approximately 6N of the high pressure fuel turbopump (HPFTP), and finally 72N frequency of the engine fuel flowmeter. One very promising feature displayed in the overlay is the strong correlation between the coincidence of FFM 72N and HPFTP 6N frequency with observed flow ratio excursions. Planar acoustic wave interaction with such a high order straightener vane harmonic was quite unexpected. The associated blossom in FFM acceleration being most dominant in the duct radial degree of freedom was unanticipated as well. A similar frequency coincidence was observed at roughly this same time between FFM 36N and what appears to be an unrelated lower frequency acoustic phenomenon. Higher fidelity duct instrumentation arrays have been proposed for future SSME ground tests to better understand the postulated duct dynamics inducing the observed flowmeter shifts.

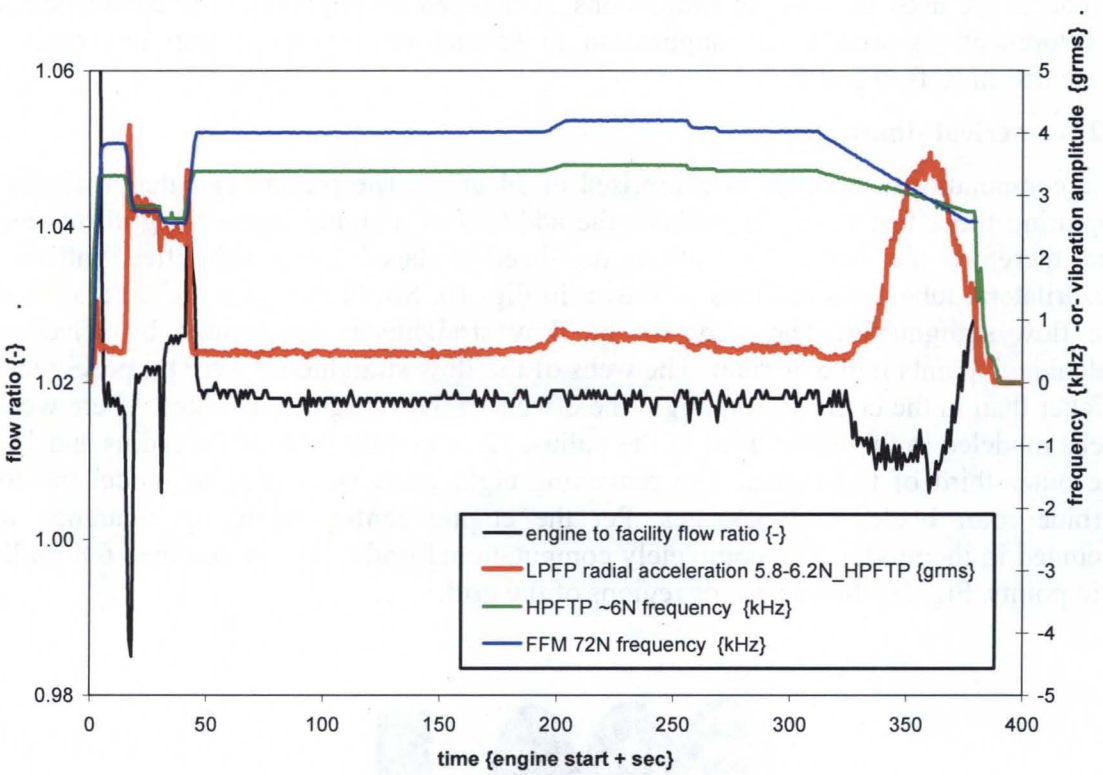

Figure 9. Postulated Interaction of LPFD Acoustic Activity with FFM Guide Vanes Producing FFM Shift

5. CFD Simulations

Numerical simulations addressing the entire flow physics have been performed with the objective of obtaining the full description and mechanism of the shifting effect due to acoustic pressure waves. The calculations captured the full two-way coupling between the rotor and the flow-field discharged by the flow straightener, calculated the rotor speed by numerically solving equation (1) at every time iteration and modeled the additional effect of acoustic pressure wave disturbance.

5.1 Numerical Method

The code used to perform the simulations is PHANTOM, a code developed at NASA Marshall Space Flight Center. The governing equations in the PHANTOM code are the three-dimensional, unsteady, Navier-Stokes equations. The equations have been written in the Generalized Equation Set format, enabling it to be used for both liquids and gases at operating conditions ranging from incompressible to supersonic flow [9]. The code employs a system of overset O-grids and H-grids to discretize the flow field. The grids move to simulate blade motion. A modified Baldwin-Lomax turbulence model is used for turbulence closure [10]. The code contains two options for the fluid properties. The first option is based on the equations of state, thermodynamic departure functions and corresponding state principles constructed by Oefelein [11]. The second option is based on splines generated from the NIST Tables [12]. Message Passing Interface (MPI) protocols are used for parallel simulations. A detailed description of the code/algorithm development, as well as its application to several turbine and pump test cases, is presented in Refs. 9 and 15.

5.2 Numerical simulations

The computational topology is comprised of 14 grids. The present calculation aimed at capturing the effect of wakes without the addition of a significant extra grid topology, and therefore the hexagonal pattern has been replaced by a simplified pattern of quadrilateral tube cross sections as shown in Fig. 10. Six of the grids are used to model the flow straightener. The webs of the flow straightener are formed by selectively "blanking" points in the domain. The webs of the flow straightener were purposely made thicker than in the engine to highlight the effects of the straightener wakes. There were 6 webs modeled in the lower third of the radius, 12 in middle third of the radius and 18 in the outer third of the radius. The remaining eight grids were used to model the four turbine rotor blades and passages. Per the engine configuration, tip clearance was included in the model. The completely computational grid topology contains 6.8 million grid points. Fig. 10 shows various regions of the grid.

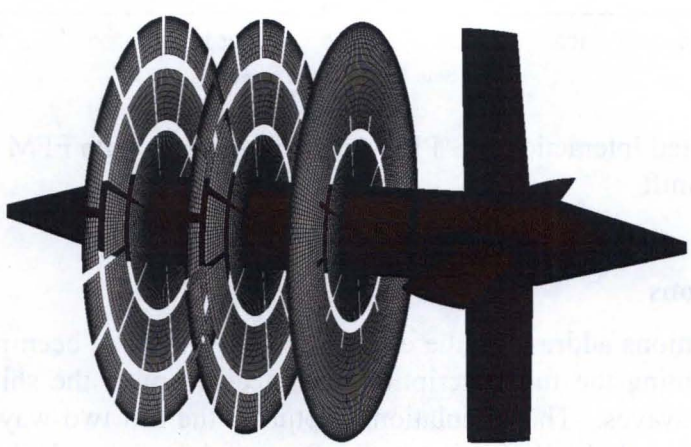

Figure 10. Computational grid for the flow straightener and turbine flow meter.

One unusual aspect of the simulations is that the rotation rate is not specified, but is calculated as part of the solution process. An initial guess is provided as input; thereafter, the predicted torque and rotor inertia are used at each time step to determine the change in the rotation rate.

The operating fluid in the flow meter is liquid hydrogen at a temperature of 42.3 degrees R and a pressure of 255 psi. The flow rate is approximately 108 lbm/sec. The process used to study the performance of the flow meter was:

1. Obtain a steady/periodic rotation rate for the rotor using specified mass flow boundary conditions at the inlet and exit
2. Using the exit pressure calculated in step 1, switch the boundary conditions to a specified exit static-to-inlet total pressure ratio and run until all transients are eliminated
3. Specify pressure waves of various amplitudes and frequencies to model the disturbances generated by the downstream pump
4. Repeat the process with the flow straightener removed to asses the effects of the straightener wakes

Figure 11 shows instantaneous static pressure contours on the hub and rotor surfaces, as well as velocity contours in selected cutting planes. The wakes generated by the web of the flow straightener, and their interaction with the passing rotor blades, are clearly visible. The wakes from the straightener persist well downstream of the turbine rotor but, as noted above, the webs were purposely made thicker than in the engine to highlight the wake effects.

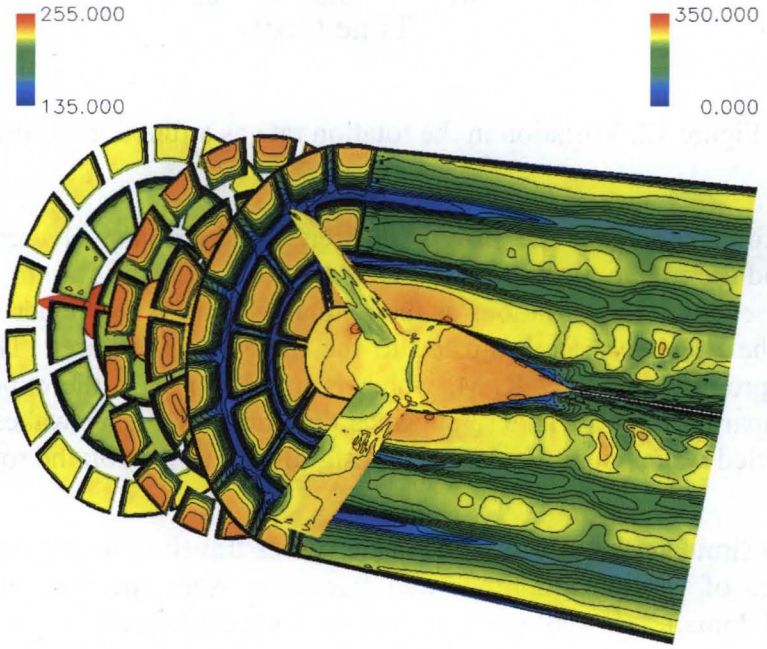

Figure 11. Instantaneous static pressure (psi) and velocity (ft/sec) contours.

Figure 12 shows the variation of the rotor rotation rate with time. The rotation speed rapidly decreases from the initial guess (and expected approximate final value) of 2400 RPM to approximately 1295 RPM. The rapid and substantial drop in the RPM is directly attributable to thickness of the straightener wakes. When a periodic state is reached, the rotation rate varies by approximately 85 RPM as the rotor moves in and out of the wakes, which confirms the initial calculation result shown in Figure 5b.. The use of specified mass flow or pressure ratio boundary conditions had only minor effects on the prediction rotation rate.

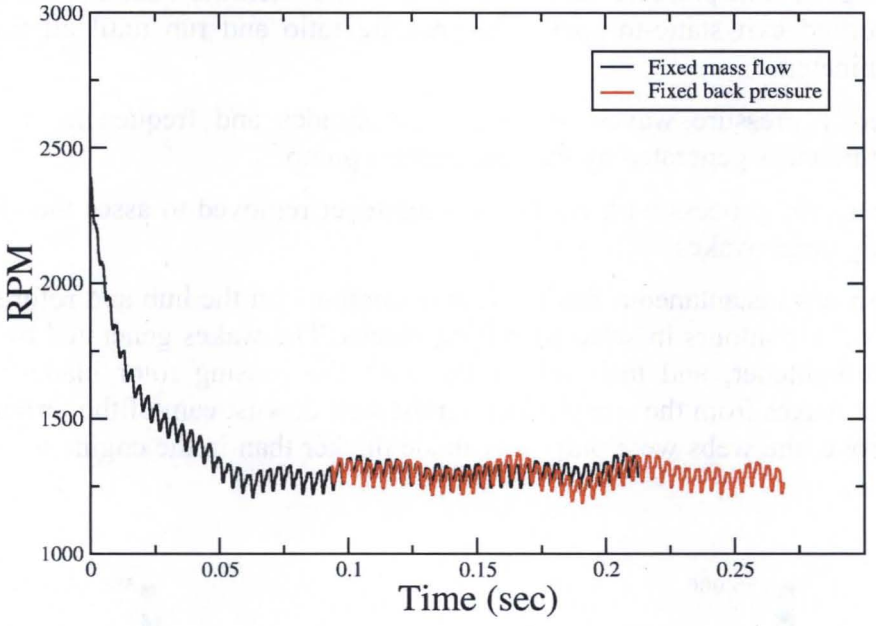

Figure 12. Variation in the rotation rate as a function of time.

As a datum for comparison the flow straightener was impulsively removed from the simulation, and the rotation rate was again allowed to reach equilibrium. The rotor speed went through several large variations as the remnants of the straightener wakes exited the domain and the flow upstream adjusted to the increased flow area. The final rotation speed was approximately 2507 RPM, which is much closer to the expected value (see Fig. 13). Comparing Figs. 12 and 13 suggests that the straightener wakes in general, and the thick modeled wakes in particular, have a significant impact on the rotation rate of the turbine rotor.

In an effort to simulate the effects of acoustic waves traveling upstream from the pump, pressure waves of varying amplitude and frequency were specified at the exit of the computational domain. The exit pressure was varied according to:

$$Pexit = P\,(\,1 + A \sin(\omega\, t + \varphi))$$

where P is the undisturbed local pressure at the exit, A is the amplitude of the specified wave, ϕ is frequency of the variation, t is time and φ accounts for any phase shift. Introducing waves at frequencies of 12N and 23N of the nominal rotation speed, and at an amplitude of 1 psi, in the simulation without the flow straightener did not generate any significant changes in the turbine rotation speed. In the simulation with the flow straightener, waves were again introduced at frequencies of 12N and 23N of the nominal rotation speed. The 12N frequency was chosen because of the 12 webs in the middle third of the flow straightener, while 23N was chosen because it does not align with any of the flow straightener frequencies. The amplitude of the 23N wave was set to 1 psi, while amplitudes of 1 psi and 10 psi were tested with the 12N wave. Figures 13 and 14 show the rotation rate as a function of time with the specified pressure waves. Interrogation of the traces shows that the 23N wave and the 12N wave at an amplitude of 1psi have little effect on the predicted rotation rate. The 12N wave with an amplitude of 10 psi, however, does have a significant effect on the rotation rate. The impact of the 10 psi wave can be quantified by looking at the average rotation rate (see Table 1). The average rotation rate for the case with the 10 psi 12N wave is nearly 25 RPM greater than that of the other three cases.

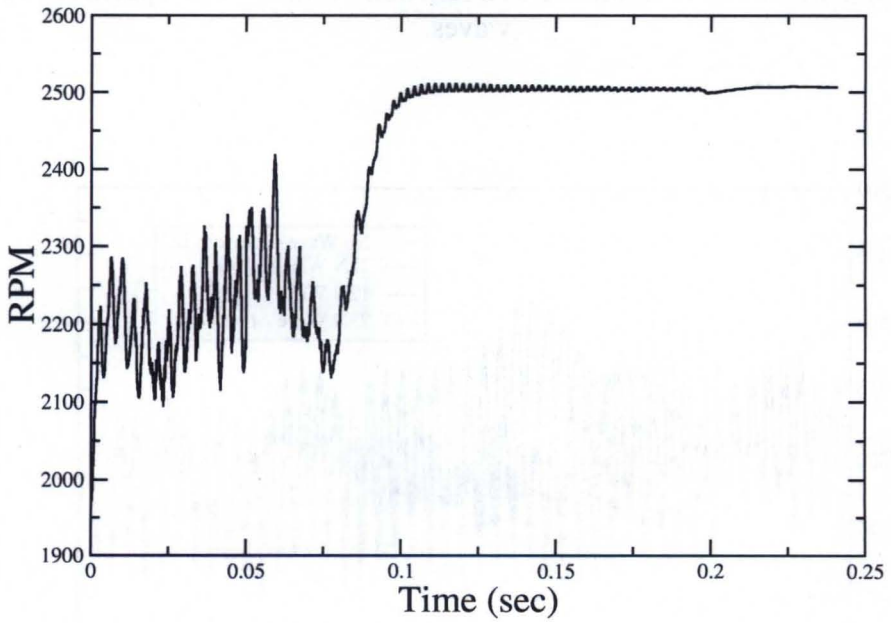

Figure 13. Variation in the rotation rate as a function of time – no straightener.

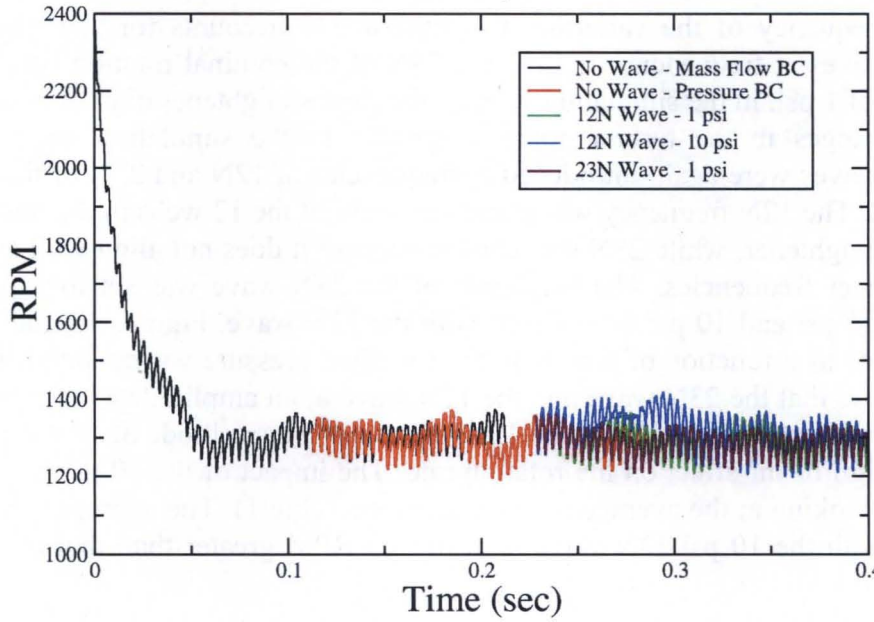

Figure 14. Variation of rotation rate as a function of time – with specified pressure waves.

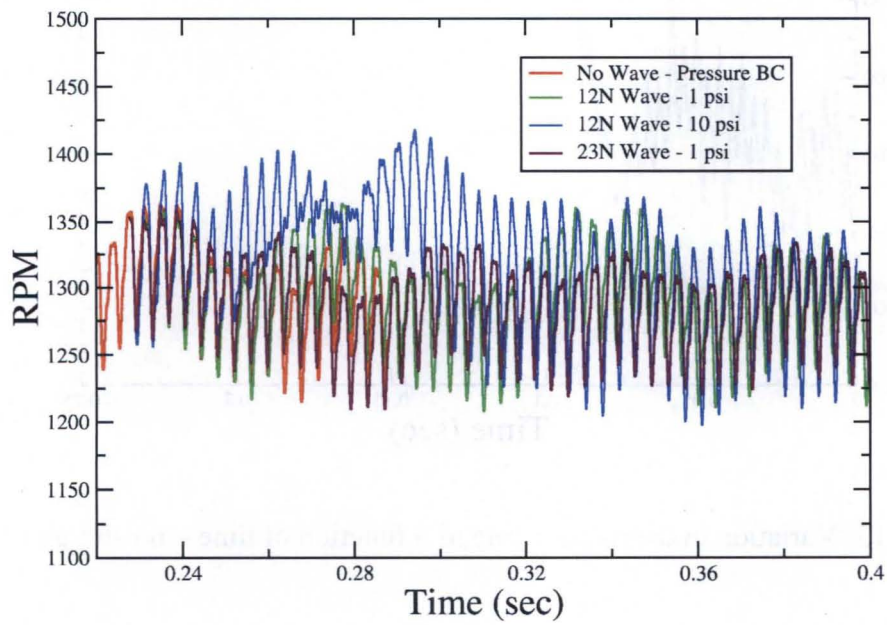

Figure 15. Close-up of rotation rate as a function of time – with specified pressure waves.

Case	Average RPM
No Wave – Pressure BC	1295
23N Wave – 1 psi	1292
12N Wave – 1 psi	1295
12N Wave – 10 psi	1319

Table 1. Average rotation rates.

The source of the RPM increase was investigated by interrogating the data from numerical probes at various points in the flow field. One location of particular interest was just downstream of the flow straightener web (but upstream of the rotor) at 67% of the duct radius. Figure 16 shows the unsteady pressure at this probe as a function of time. The time at which the pressure wave reaches the probe is clearly evident in Fig. 16. The amplitude if the wave is approximately 80% of its original value at this location. The frequency content of the unsteady pressure at the probe is predominantly 12N, with much smaller contributions at the rotor blade passing frequency and its harmonics.

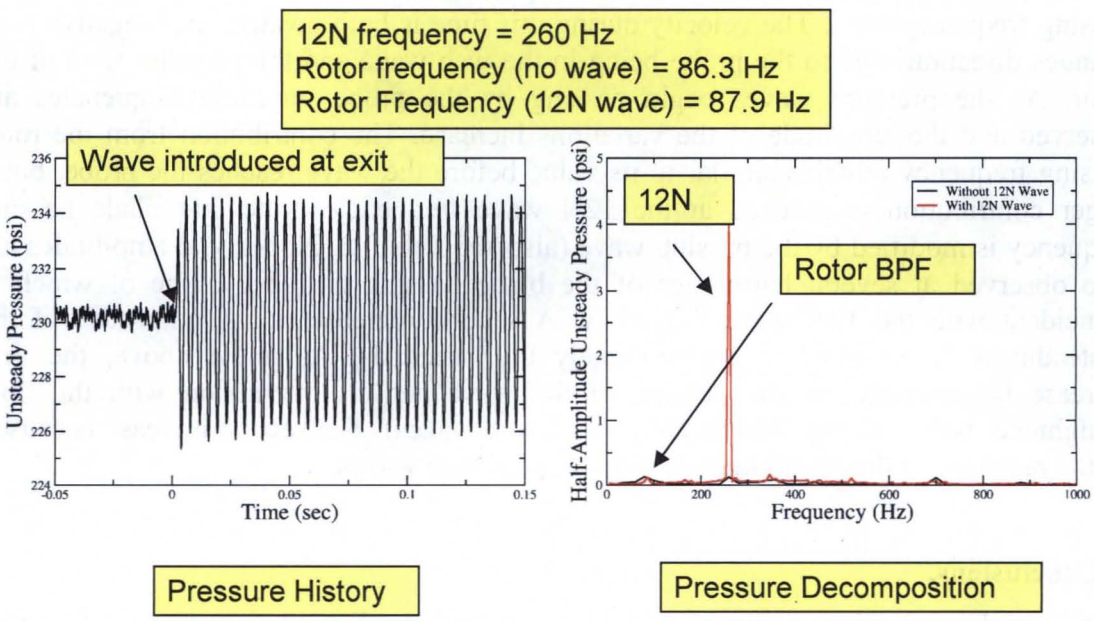

Figure 16. Variation of the static pressure (psi) as a function of time.

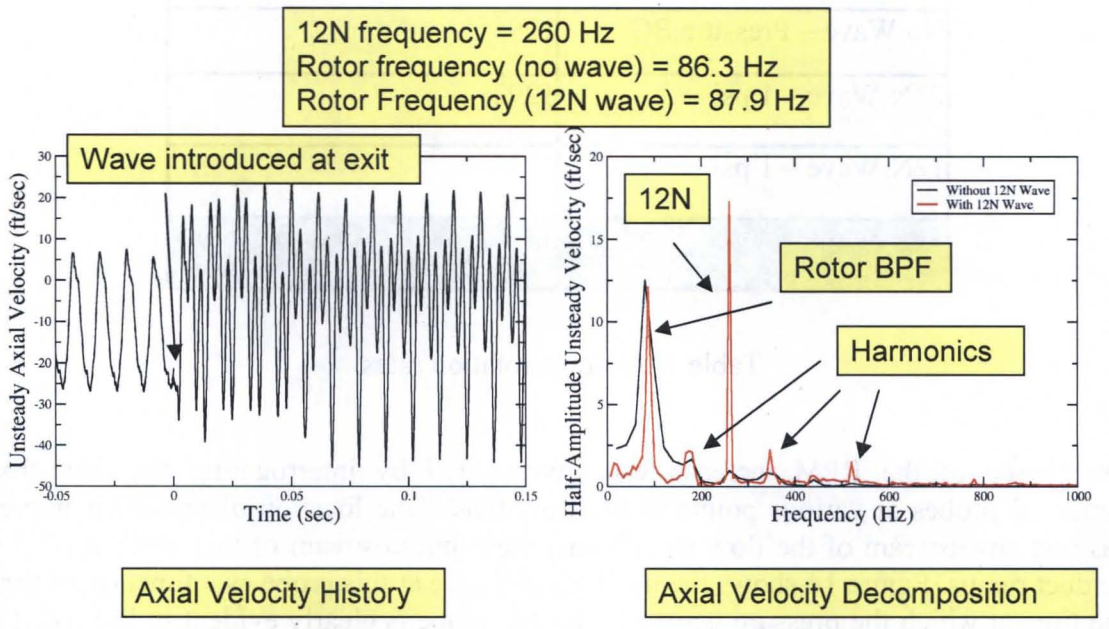

Figure 17. Variation of the axial velocity (ft/sec) as a function of time.

Figure 17 shows the variation of the axial velocity at the probe as a function of time. In the time before the pressure wave reaches the probe, the velocity varies at the rotor blade passing frequency (4N). The velocity during this time is both positive and negative (i.e., changes direction) due to the probe being in the web wake and the pressure field of the rotor. As the pressure waves begin passing by the probe, multiple frequencies are observed and the amplitude of the variations increase. The contribution from the rotor passing frequency remains similar to its value before the wave reaches the probe, but a larger contribution is induced at the 12N wave frequency. Note that blade passing frequency is modified by the passing wave (also see Table 1). Non-trivial amplitudes are also observed at several harmonics of the blade passing frequency, one of which is coincident with the 12N wave frequency. A second increase in the amplitude of the unsteadiness is observed at approximately 0.07 seconds. As noted above, the first increase is generated by the passing of the wave and its interaction with the flow straightener web (i.e., the modification of the web wakes). The second increase is caused by the response of the rotor blades to the modified web wakes.

6. Conclusions.

A potential mechanism for generating sudden and random shifts in the calibration constant of the Space Shuttle Main Engine Fuel Flow Meter has been investigated using simple theoretical models and algorithms leading up to a complex 3-D CFD analysis. While the latter analysis is being continued further, preliminary results support the hypothesis that the interaction between the wakes generated by the FFM's flow

straightener and acoustic plane pressure waves matching harmonics of the flow straightener vane passing frequencies can generate a change in the average rotor speed without any modification of the volumetric flow value. Further work is required in order to understand the complete mechanism and to quantify the limits of its magnitude. The result of the work presented is significant for liquid propellant rocket engine health management systems requiring real time measurement of propellant flows. The authors appreciate that the calibration shift mechanism analyzed may not be the only combination of factors generating the observed behavior. However, it is one that has appears to have a sufficient number of factors in place to explain at least some of FFM's observed operational behaviors .

Acknowledgements

The authors would like to thank Lisa Griffin, Alisa Shivers, and Katherine Van Hooser of the George C. Marshall Space Flight Center and Curtis Davis and Dan Fellbaum at Pratt & Whitney Rocketdyne for their support of this investigation. The authors would also like to thank their colleagues Greg Frady, Doug Lynch, Bruce Maynard, Munir Merchant, John Ubowski and Jerit Wendlandt for valuable technical discussion.

References

1. J.T. France, "The Measurement of Fuel Flow", AGARD Flight Test Instrumentation Series, Volume 3, NATO publication, 1972.
2. Fenwick, J.R., "Discussion of the SSME Fuel Flowmeter Anomaly", Rocketdyne Internal Report, October 13, 1993.
3. Fox. T.H., "Possible Mechanism for Flowmeter Oscillations Seen on STS-8", Mashall Space Flight Center Letter, April 9, 1984
4. L. K. Sharma, "Fuel Flowmeter Problem: Drop in Calibration Constant with Power Level", Rocketdyne Internal Report, May 13, 1988.
5. Ascoli, E. et. al. "Application of CFD to Explain Stall Behavior of the SSME Flowmeter", AIAA paper 99-2458, presented at the 35th AIAA/ASME/SAE/ASEE Joint Propulsion Conference and Exhibit.
6. Hadid, A. "Transient CFD Analysis of the SSME Fuel Flowmeter Anomaly" Rocketdyne Internal Report, May 5,1998.
7. Schlichting, H. "Boundary Layer Theory", McGraw Hill, 1979
8. Abbot, I.H. and von Doenhoff, A. E.," Theory of Wing Sections", Dover , 1949.
9. Sondak, D. L. and Dorney, D. J., "General Equation Set Solver for Compressible and Incompressible Turbomachinery Flows," AIAA 2003-4420, 39th AIAA/ASME/SAE/ASEE Joint Propulsion Conference and Exhibit, Huntsville, AL, July 20-23, 2003.

10. Baldwin, B. S., and Lomax, H., "Thin Layer Approximation and Algebraic Model for Separated Turbulent Flow,'' AIAA Paper 78-257, Huntsville, AL, January, 1978.

11. Oefelein, J. C., Sandia Corporation, Livermore, CA, Private Communication, December, 2002.

12. http://webbook.nist.gov/chemistry/fluid

13. Merkle, C. L., Feng, J.-Z., and Buelow, P. E. O., "Computational Modeling of the Dynamics of Sheet Cavitation, " Third International Symposium on Cavitation, Grenoble, France. April, 1998.

14. Ahuja, V., Hosangadi, A., and Ungewitter, R. J., "Simulations of Cavitating Flows in Turbopumps," AIAA 2003-1261, 41st AIAA Aerospace Sciences Meeting & Exhibit, Reno, NV, January 6-10, 2003.

15. Dorney, D. J., and Sondak, D. L., ``Application of the PHANTOM Analysis to Impeller and Diffuser Geometries," 52nd JANNAF Propulsion Meeting, Las Vegas, NV, May 10-13, 2004.